
Article:
Muller, C, Biggs, J, Ebmeier, SK orcid.org/0000-0002-5454-2652 et al. (5 more authors) (2018) Temporal Evolution of the Magmatic System at Tungurahua Volcano, Ecuador, detected by geodetic observations. Journal of Volcanology and Geothermal Research, 368. pp. 63-72. ISSN 0377-0273

https://doi.org/10.1016/j.jvolgeores.2018.11.004

Temporal Evolution of the Magmatic System at Tungurahua Volcano, Ecuador, detected by geodetic observations

Cyril Muller[a,b,*], Juliet Biggs[b], Susanna K. Ebmeier[c], Patricia Mothes[d], Pablo B. Palacios[d], Paul Jarrin[d], Marie Edmonds[e], Mario Ruiz[d]

[a] *Observatorio Vulcanológico y Sismológico de Costa Rica, Universidad Nacional, 2346-3000 Heredia, Costa Rica*
[b] *School of Earth Sciences, University of Bristol, Wills Memorial Building, Queen's Road, BS8 1RJ Bristol, U.K.*
[c] *School of Earth and Environment, University of Leeds, LS2 9JT, UK*
[d] *Instituto Geofísico de la Escuela Politécnica Nacional, Ladrón de Guevara E11-253, Quito, Ecuador*
[e] *Earth Sciences Department, University of Cambridge, Downing Street, Cambridge, CB2 3EQ, UK*

Abstract

Changes in the pathway and timescale of magma ascent can be responsible for variations in eruptive style during long-lived eruptions, but are only documented at a small number of well-instrumented systems. Here we integrate PS-InSAR from high resolution TerraSAR-X radar imagery with continuous GPS data from 4 sites at Tungurahua volcano, Ecuador. Our results show long-term uplift between 2011-2014 associated with a continuously inflating prolate spheroid reservoir at a depth of ~ 10 km beneath the summit. Comparisons with eruptive flux, taking compressibility into account, suggest that during this time period slightly over half the magma supplied to the system was erupted. The observations span three distinct phases of eruption and in 2012-2013, an increase in eruptive activity was accompanied by uplift on the volcano's western flank. Similar episodes have previously been observed during large Vulcanian eruptions and we attribute them to intrusions into an area of mechanical weakness. A localised patch of subsidence mid-way up the Tungurahua's western flank is

*Corresponding author
Email address: cyril.muller21@gmail.com (Cyril Muller)

co-located with a swarm of shallow long-period seismicity and may represent a potential site for a development of a lateral vent. This study demonstrates that satellite geodetic techniques are capable of characterising the geodetic signature of transitions in eruptive style during long-lived andesitic eruptions even where deformation is low magnitude and measurements are challenging.

Keywords: `Tungurahua, volcano, InSAR, GPS, statistical integration`

---

1. Introduction

The nature of volcanic eruptions is controlled by the supply rate and composition of the magma, and the geometry of the plumbing system (Sparks, 2003). Geophysical and geochemical observations, such as seismicity, surface deformation and SO_2 flux can be used to study the patterns of magma ascent and storage and hence forecast eruptive activity (Sparks, 2003; Biggs et al., 2014; Phillipson et al., 2013). During long-lived andesitic eruptions, a major challenge is to forecast changes in behavior, and in particular, the transition from semi-continuous eruptions and low explosivity to larger explosive eruptions. In this work, we address this challenge by using geodetic techniques to detect the geometry of the plumbing system at Tungurahua volcano, Ecuador, its temporal evolution, and changes in eruptive behavior.

Tungurahua volcano in Ecuador has been erupting since 1999 (Mothes et al., 2015), with activity varying from Strombolian to sub-Plinian. Continuous eruptive phases last from several weeks to more than a year (Hidalgo et al., 2015), with hiatuses lasting weeks to months. In this study, we use geodetic data from GPS (Global Positioning System) and InSAR (Interferometric Synthetic Aperture Radar) to detect long term and transient deformation. We apply stacking and Persistent Scatterer methods to high-resolution InSAR images acquired by the TerrSAR-X satellite between May 2011 and April 2014. We then combine these methods with GPS total displacements to produce a 3D velocity map. The integration of the geodetic data provides a unique insight into the temporal

and spatial characteristics of the deformation processes, allowing us to identify a continuously-inflating deep reservoir and an intrusion event into the edifice.

2. Tungurahua volcano

2.1. Geological background and current activity

Tungurahua volcano in Ecuador is a 3000 m relief, active andesite stratovolcano with a summit at 5023 m above mean sea level (a.m.s.l.). It is located in the eastern Cordillera of the Ecuadorian Andes, which is bordered to the west by the ∼30-50 km wide inter-Andean valley and to the east by the Amazonian rear-arc lowlands. The edifice was built in three main constructive periods, interrupted by two flank failure events (Hall et al., 1999). The large amphitheatre on the western flank was created by the last collapse, 3000 years ago and is now filled with weak unconsolidated material (Molina et al., 2005).

The ongoing eruption started in 1999, after eight decades of inactivity. The activity since 1999 is extremely variable, alternating between short hiatuses, forceful gas explosions, ash emissions and lava fountaining (Mothes et al., 2004), with 4 VEI2 events and one VEI3. The VEI3 eruption in August 2006 generated an ash column which rose over 16 km above sea level, pyroclastic flows that covered half of the western cone, reaching the surrounding drainages (Kelfoun et al., 2009) (Fig. 1) and ash fall of more than 10 cm on the south-western part of the edifice (Eychenne et al., 2013) (Fig. 1).

Between July 2009 and July 2014, the volcano experienced 3 distinct periods of behaviour (Hidalgo et al., 2015) (Fig. 2 and Fig. 3). Period 1, from July 2009 to November 2011, was characterized by highly explosive eruptions with well-defined starts and ends. The eruptive episodes were spaced 4 to 6 months apart, and each lasted between a month and two months. Period 2, between December 2011 and August 2012, was characterised by continuous, low-level

Strombolian explosions and ended with a Vulcanian explosion on August 21^{st} 2012 (Mothes et al., 2015). This period lasted 9 months with only a few days of hiatus. Period 3, from September 2012 to July 2014, was again a period with well-defined explosions and at least 5 Vulcanian eruptions. The eruptions lasted between 2 weeks and a month with only one or two months between them.

2.2. Geophysical and Geochemical Monitoring

Tungurahua is monitored by the Instituto Geofísico de la Escuela Politécnica Nacional (IG-EPN), which runs seismic, tiltmeter and GPS networks (Alvarado et al., 2018) as well as scanning mini-DOAS (Differential Optical Absorption Spectrometers) (Arellano et al., 2008; Kumagai et al., 2007; Palacios et al., 2015; Hidalgo et al., 2015; Neuberg et al., 2018). SAR images are made freely available through the GEO Ecuadorian Volcano Supersite (http://supersites.earthobservations.org/ecuador.php). The seismicity is dominated by swarms of Long Period (LP) and explosion events, which are generally correlated with eruptions (Fig. 2). Few volcano-tectonic (VT) earthquakes are recorded, but those that do occur are mainly located on the western flank (Palacios et al., 2015). An increase in VT events between mid-2012 and early 2013 corresponded to the transition between the second and third phases. (Molina et al., 2005). SO_2 flux correlates with eruption explosivity (Hidalgo et al., 2015), with 95% of the total emissions occurring during eruptive phases and fluxes of <100 tons per day (t/d) otherwise (Hidalgo et al., 2015). During periods of low explosivity (e.g. November 2011 to September 2012) the average SO_2 flux was 700 t/d and during high explosivity phases the flux averaged 1400 t/d. Prior to 2008, long periods of low explosivity were the norm and the system was considered open, but after 2008, more explosive, episodic eruptions and eruptive phases have been attributed to closed-system behaviour (Hidalgo et al., 2015).

In 2008, InSAR detected uplift of up to 17.5 cm on the upper western flank of Tungurahua, attributed to a sill-like intrusion within the volcanic edifice coincident with a Vulcanian eruption (Biggs et al., 2010b). Subsequently, a Persistent

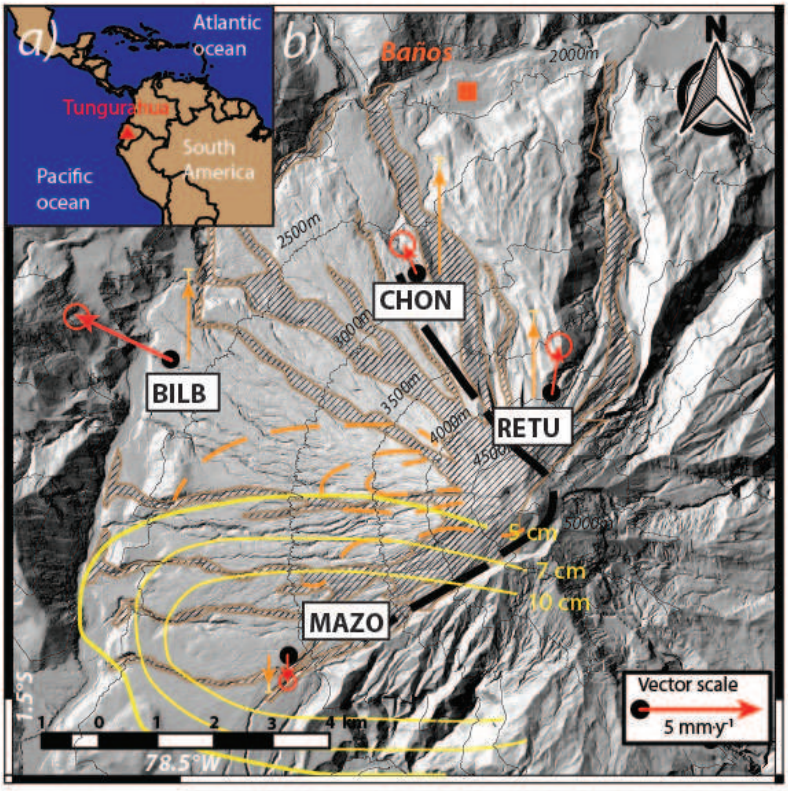

Figure 1: The location and geological setting of Tungurahua volcano. a) the location of Tungurahua in the western South American continent. b) Tungurahua volcano edifice, including 2006 surge deposits described by Kelfoun et al. (2009), which are indicated by the brown hatched areas. The dashed orange contours are the InSAR deformation detected by Biggs et al. (2010b) in centimetres. The thick black dashed line is the surface expression of interface of the last flank failure from Hall et al. (1999). The contours of the ash fall thickness from the August 2006 eruption from Eychenne et al. (2013) are in yellow. The red and orange arrows shows the average horizontal and vertical velocities, respectively, of the GPS sites between May 2011 and March 2014 (when the TerraSAR-X imagery was acquired).

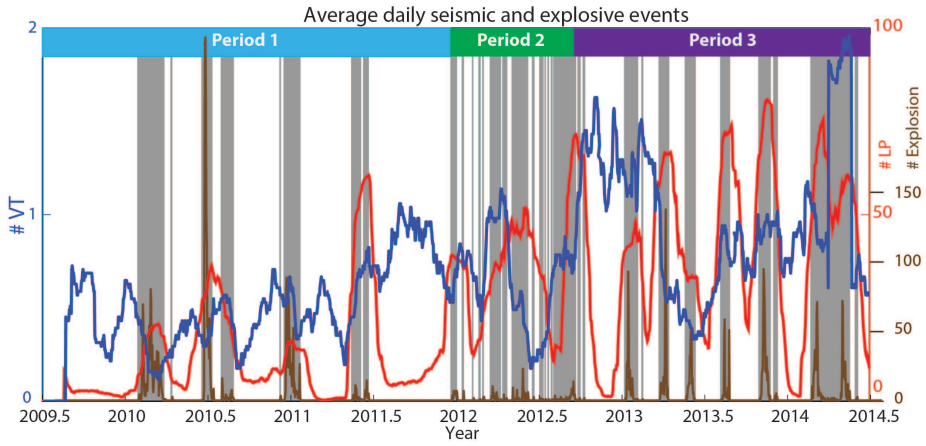

Figure 2: Daily number of Volcano-Tectonic (VT), Long Period (LP) and explosive events detected by the Instituto Geofísico seismic network. A centred moving average with a window of 50 days has been applied to the VT (blue line) and LP (red line) counts. The brown line shows the number of explosions per day, while the grey bars indicate days on which at least one sub-aerial explosion occurred. The three different periods with different eruptive behaviour identified by Hidalgo et al. (2015).

Scatterer (PS) study using ENVISAT SAR data between 2003 and 2009 found continuous uplift over a 25 km-radius area, centered on Tungurahua (Champenois et al., 2014). The deformation of up to 8 mm·y^{-1} is best modeled by a continuously replenishing reservoir seated at 11.5 km below sea level, or 14 km below average surface. Champenois et al. (2014) found few persistent scatterers on the edifice itself, so that dataset is insensitive to shallow sources of deformation. Short-term cycles of ground tilting interpreted as the product of conduit shear stress were also detected before eruptions by a single tiltmeter, RETU, located within 2 km of the volcanos summit (Neuberg et al., 2018).

3. Methods

3.1. InSAR and StaMPS

TerraSAR-X is a right-looking X-band SAR satellite operated by the Deutsches Zentrum für Luft- und Raumfahrt (DLR). We use 41 images from May 13th 2011

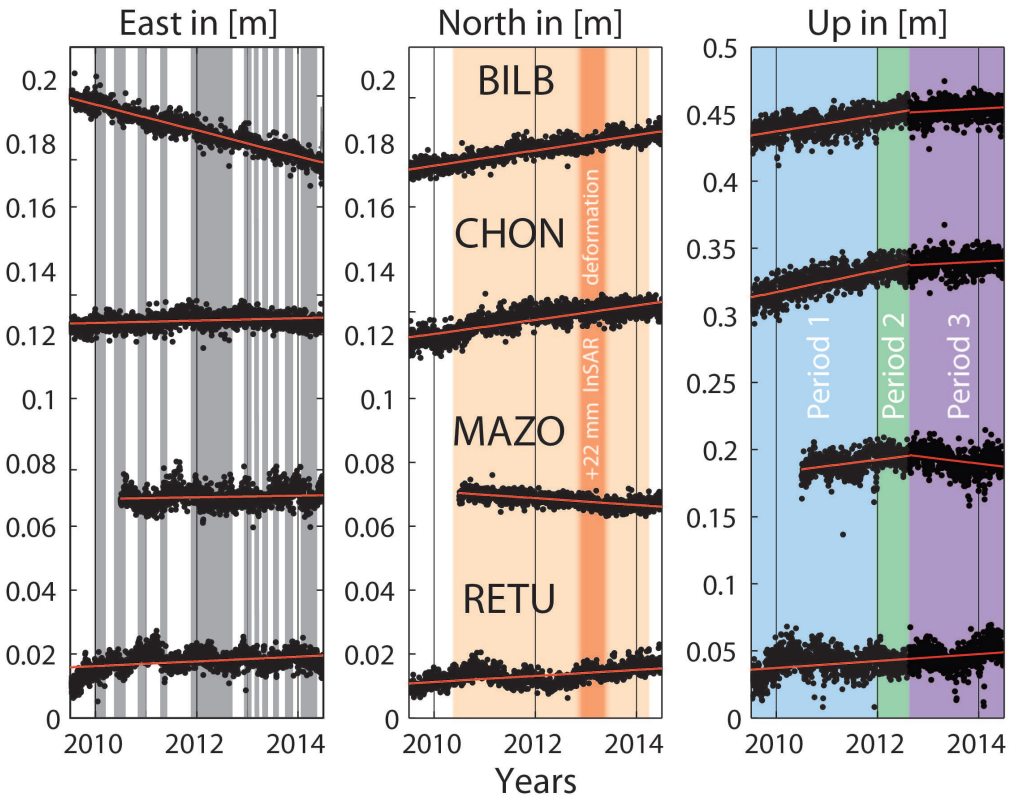

Figure 3: GPS time series from mid-2009 to mid-2014. The black dots are the daily GPS solutions for the North, East and vertical components. The red lines show the trend of each time series. At the end of the Period 2, the vertical time series of BILB, CHON and MAZO GPS sites show a >4 mm·y^{-1} change in the trend (see Results section). The East subplot, the grey rectangles denote eruptive periods from Hidalgo et al. (2015). The North subplot, the light orange rectangle show the period of InSAR acquisition, while the darker orange rectangle show the period when +22 mm InSAR deformation have been detected. The vertical subplot shows the three different periods with different eruptive behaviour identified by Hidalgo et al. (2015).

to March 1^{st} 2014. The satellite has a wavelength of 31 mm, and high spatial resolution of 1 m, but coherence is rapidly lost in vegetated areas (e.g. Ebmeier et al., 2013). Tungurahua is a steep-sided stratovolcano, so, the western flank is better imaged by descending satellite passes and the eastern flank by ascending passes. Recent eruptive deposits cover the western flank, which is consequently less vegetated than the eastern flank. TerraSAR-X has a repeat orbit of 11 days, but intervals between successive acquisitions vary between 11 days and months depending on the satellite acquisition schedule. Interferograms were processed using the ROI-PAC software (Rosen et al., 2004) and topography was removed with a 5 m resolution Digital Elevation Model acquired from an airborne LiDAR (Light Detection And Ranging) mission ordered by IG-EPN.

Individual interferograms are dominated by stratified tropospheric noise associated with the high relief edifice (3-5 cm) (e.g. Parker et al., 2015; Ebmeier et al., 2013) so we combine interferograms to improve the signal-to-noise ratio (Biggs et al., 2010a; Berardino et al., 2002; Hooper et al., 2007). First, we stack the common coherent parts of each interferogram using the assumption that noise is random but this results in very limited spatial coverage (Fig. 4a).

Next, we apply the Persistent Scatterer (PS) method (Hooper et al., 2007), which uses amplitude dispersion (Ferretti et al., 2001) and the stability of the phase of each pixel to select persistent scatterers which are then used for further analysis (Hooper et al., 2009; Riddick et al., 2012; Pinel et al., 2011). First, the raw images and interferograms are computed relative to a common master image, and then in a series of iterations, the algorithm identifies the candidate pixels that have persistent scattering characteristics through time. The spatial correlation characteristics of the signal are then used to reduce the noise due to orbital and atmospheric errors. We chose the January 29^{th} 2013 acquisition as the master image because it is in the middle of our period of study. The spatial coverage is limited by the DEM rather than the SAR images. We obtain 24,541 persistent scatterers mainly located at the foot of the volcano, although

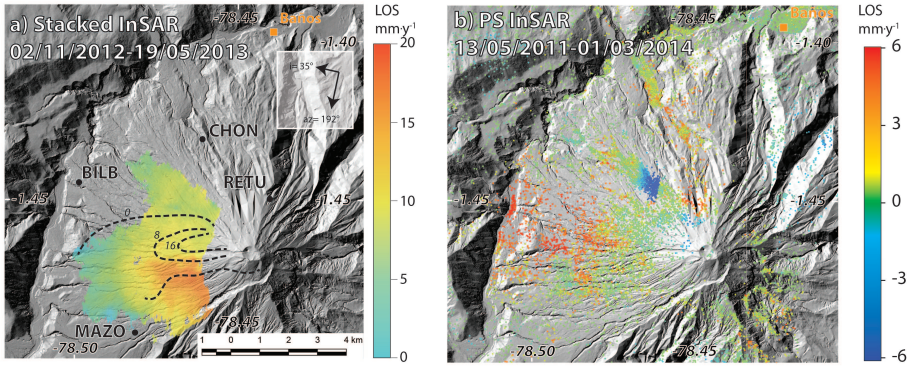

Figure 4: InSAR observations from TerraSAR-X track 142. a) displacement from stacked interferograms between November 2^{nd} 2012 and May 19^{th} 2013. The black dashed contours show the early 2008 co-eruptive displacements in cm from Biggs et al. (2010b). Within the white box, the arrows with a value in degrees are the orbital heading and incidence angle of track 142 used for both insets. The black dots show the position of the 4 permanent GPS sites. b) velocities from InSAR Persistent Scatterers analysis using StaMPS for the May 2011-March 2014 period.

a significant number are situated on the edifice itself (Fig. 4b). The root mean square error (RMSE) on velocity is between 0.4 and 2.1 mm·y^{-1} .

3.2. Integration of GPS and InSAR

InSAR has a high spatial coverage but low temporal resolution and measures velocity only in the line-of-sight (LOS) of the satellite, while GPS measures 3 components of displacement in an absolute reference frame, but at a sparse network of sites. Combining InSAR and GPS takes advantage of the benefits of each approach, and can be used to produce a 3-D displacement or velocity field (Samsonov and Tiampo, 2006; Guglielmino et al., 2011; Muller et al., 2015).

In 2009-2010, four permanent GPS stations were installed at Tungurahua. RETU on the northern flank is at 3900 m above mean sea level (m.s.l.); MAZO and CHON on the south-western and north-western flank are at elevations of 2900 and 2800 m above m.s.l. respectively and BILB is located on the foot of the western flank at 2300 m above m.s.l.(Fig. 1). Daily positions of the GPS

sites are computed with GAMIT/GLOBK software (Herring et al., 2010) (Fig. 3). The fiducial site, RIOP, located 39 km south-west of the volcano, is used to remove the tectonic signal and most of the atmospheric artefacts. The RMSE of the vertical and horizontal GPS velocities is below 2 millimetre per year for all the sites at 95% confidence.

We use the continuous medium method of Guglielmino et al. (2011) to combine InSAR and GPS measurements. This method has provided reliable results on volcanoes (Guglielmino et al., 2011; Muller et al., 2015). The 3D velocity vector, v_P, and gradient tensor, $\mathbf{H}$, are computed for each pixel P using: 1) the InSAR velocities $\mathbf{v_m}$ at the pixel P; 2) its 3D position, $\mathbf{x_p}$ from a DEM and 3) the velocities $\mathbf{v_n}$ of the n surrounding GPS sites. The stochastic model accounts for the accuracies of each observation, weighted according to the distance between the computed pixel P and the n GPS sites as necessary. At Tungurahua, there are 4 GPS sites spread around the western flank of the volcano, while the InSAR data cover most of the edifice. Our results are most reliable in areas of both good InSAR and GPS coverage. However, there are some areas without GPS coverage where the 3D deformation field is poorly constrained. These are identifiable from high RMS errors reflecting the mismatch between GPS and InSAR.

GPS velocities are available from July 2009 whereas TerraSAR-X images are only available from May 2011. Therefore, we use the mean velocity of both GPS and InSAR over the May 2011-March 2014 period to generate a integrated deformation field (Fig. 5). To downsample the InSAR, we create a 100 m x 100 m grid and compute the velocity for each pixel that contains at least one PS. When several PS were available in the same pixel, we use their accuracy to calculate a weighted average of the deformation rate. The InSAR data are shifted to agree with the GPS velocities projected in the LOS velocity to make use of the absolute reference frame provided by the GPS network, following Muller et al. (2015). Using the average velocity from both GPS and

Table 1: Averaged velocities for the GPS sites for the mid-2009 to mid-2014 period and when InSAR data were acquired from May 2011 to March 2014. RMS velocity errors <2 mm at 95% confidence.

	July 2009 - July 2014			May 2011- March 2014		
Site	East	North	Up	East	North	Up
			[mm·y^{-1}]			
BILB	-4.1	2.4	4.2	-4.0	1.9	3.2
CHON	0.4	2.2	5.7	-0.5	1.2	4.3
MAZO	0.4	-1.0	0.5	0.3	-1.2	-1.3
RETU	0.7	1.0	1.9	0.3	2.0	3.1

InSAR observations results in a temporal smoothing of the deformation which is adequate for investigating a long-term process (e.g. replenishment of a crustal reservoir) but not for pre-eruptive or transient processes. The root mean square error of the integrated velocity field is <2 mm·y^{-1}.

4. Results

4.1. Long-term deformation (> 3 years)

The GPS displacement and velocity time series of all four GPS sites show both long-term trends and transient changes. The long term velocities make a radially outward pattern, with uplift at all the sites (Fig. 1) and larger horizontal and vertical rates at the base of the edifice than at the top (Tab 1, Fig. 3). The largest magnitude deformation in the StaMPS velocity field occurs at the base of the western flank and at a sharp-edged area of subsidence located on the western flank (Fig. 4b). A long wavelength gradient from motion away from the satellite on the eastern flank and movement towards the satellite on the western flank could be associated with orbital errors in the InSAR. However, GPS vertical velocities reveal the same trend and we conclude this signal is a displacement of the volcano surface.

The integrated velocity field between May 2011 and March 2014 shows i) radially outward displacement vectors across the entire edifice, with the pattern centred 2 km to the west of the crater, ii) the northwestern third of the edifice is dominantly uplifting with larger rates at the base of the edifice than at the summit and iii) subsidence on the eastern flank (Fig. 5). The maximum uplift of 10 mm·y^{-1} is located at the base of the edifice, close to the BILB GPS site. There are no GPS sites located on the other side of the drainage which surrounds the volcano, so the velocities in the far field have high uncertainties (label 4 in Fig 5) and we do not consider this area further.

In addition to this general pattern, we detected several deformation areas of smaller spatial coverage: on the northwestern flank, we detect a small area of subsidence (labeled 1 in Fig 5); the upper 900 m of the edifice shows subsidence of several millimetres per year (2 on Fig 5) and we observe subsidence on the eastern flank from Baños to an altitude of 4000 m (3a,b on Fig 5). The area of subsidence on the northwestern flank (labeled 1) is approximately 900 m by 600 m in extent and has a sharp boundary with the surrounding area. The boundary is sharpest in the east consistent with a trap door style motion (e.g. Amelung et al., 2000). These areas have higher RMSEs than the surrounding 3D deformation field, and the direction of the velocity should be viewed with caution.

We investigate the source parameters responsible for the large-scale, long-term uplift and radial deformation. First, we forward model the best-fit parameters from the 2003-2009 InSAR study (Champenois et al., 2014): a point source at 14.5 km below the average surface with a continuous rate of volume change of around 7 million m^3·y^{-1} (Table 2). The original model assumed the source was located directly beneath the active crater, however, our data, which include more PS points on the edifice suggests the centre of the radial pattern is 2 km further west and we adapt the model accordingly (Fig. 6). Subtracting the adapted model from our observations shows only minor residuals in the hori-

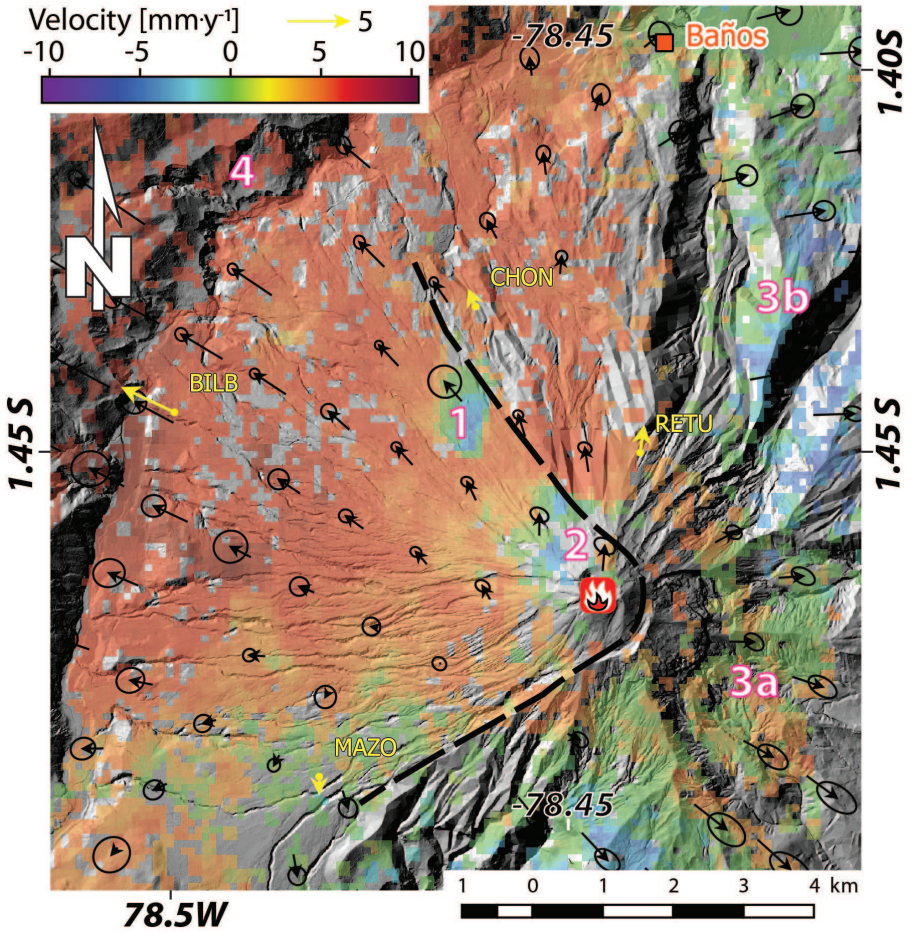

Figure 5: Integrated velocity field and its accuracy between May 2011 and March 2014 at Tungurahua volcano. The color map shows the vertical velocities, while the black arrows display the horizontal velocity and their ellipse of accuracy. Yellow arrows represent the horizontal velocities for the 4 GPS sites. The black dashed line is the avalanche caldera scar from Hall et al. (1999).The pink and white numbers show the significant residual areas on the prolate model.

zontal components (<2 mm·y^{-1}), but vertical residuals of >5 mm·y^{-1} (Fig. 6b).

Prolate spheroid source geometries generate greater horizontal to vertical displacements than a spherical or point source and are regarded as more physically realistic for a stratovolcano (Odbert et al., 2014). Using the programme dModels (Battaglia et al., 2013), the best-fitting prolate spheroid source has a 2 km long axis and 200 m short axis, inclined at an angle of 25 ° degrees toward the west-northwest (azimuth $\phi = 300°$). The depth of 7.4 km beneath the average surface or 4.9 km below m.s.l. (Table 2) and volume change of ∼2 M m^3·y^{-1}, are discussed further in section 5. The prolate shape can reproduce both the horizontal and vertical patterns of deformation: the residuals of this model are <2 mm·y^{-1} in the horizontal and mainly <1 mm·y^{-1} across the edifice. This model cannot account for the areas of subsidence described previously (1, 2, 3a and 3b in Fig. 5).

None of these models account for topography or anisotropy and need to be interpreted carefully when applied to steep-sided volcanoes such as Tungurahua, which has relief of 3000 m. The half-space assumption can cause an underestimate of volume change by a factor of up to 50% (Cayol and Cornet, 1998), corresponding to an increase of 1 Mm^3·y^{-1} for our data. Anisotropy and inelastic effects may have even greater impact on the modelled volume, depth and shape of the reservoir (Trasatti et al., 2003; Gottsmann and Odbert, 2014), but few constraints exist on these parameters at Tungurahua. Therefore, we consider the modelling to be an initial first-order approach at explaining the complex displacement field.

4.2. Medium time scale deformation (6-24 months)

We define medium time scale deformation as transient events that occur over 6 to 24 months. By stacking the InSAR data, we detect uplift of ∼2 cm high on the south-western flank during the period between November 2^{nd} 2012 and May 19^{th} 2013 (Fig. 4a); with an average rate of 4 cm·y^{-1}. To investigate this signal

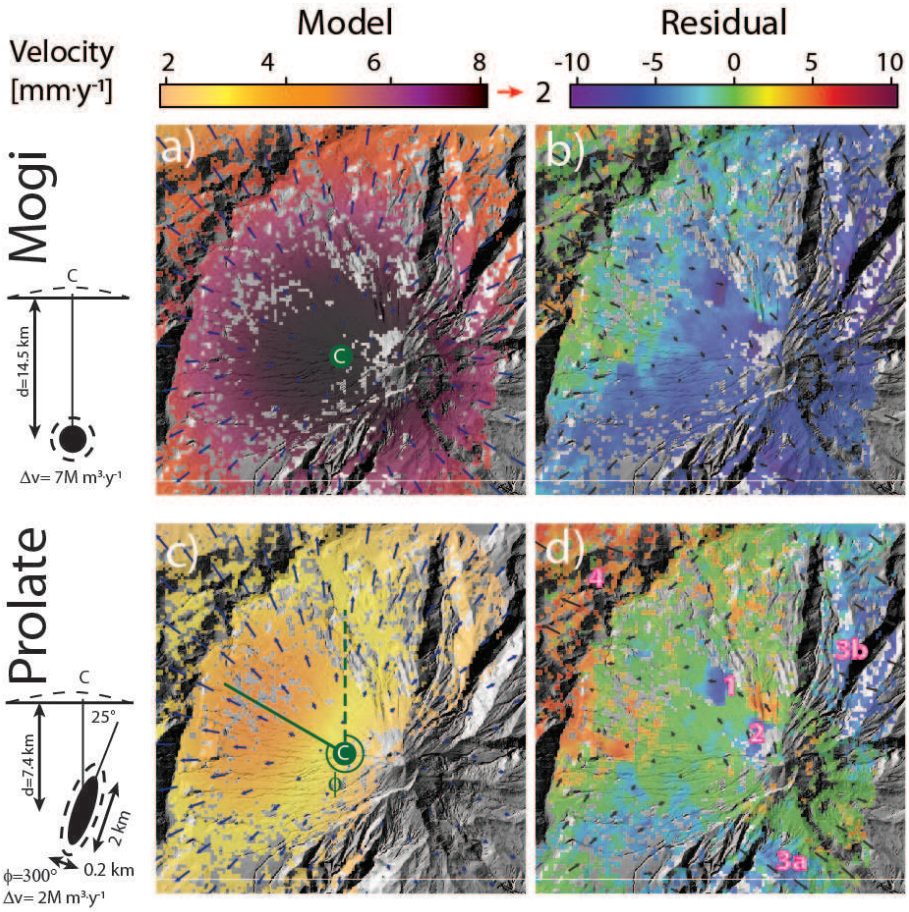

Figure 6: Results of the analytical modelling. Panels a) and b) present the predicted deformation from a Mogi model and the residual with our data. We use Champenois et al. (2014)'s parameters, but move the centre of the source westward to better fit our data. Panels c) and d) show the Yang model resulting from our best inversion. The blue arrows show the deformation implied by the models, while the grey arrows show the residuals velocity vectors. The colored map shows the vertical velocities. The letter C within the green circle shows the position of the centres of the deformation source. The pink and white numbers show the significant residual areas on the prolate model.

Table 2: Parameters of the tested models. Elastic parameters of these models are $4{\cdot}10^9$ GPa for the 1^{st} Lame constant and $6.25{\cdot}10^9$GPa for the shear modulus. χ^2 is the overall misfit, unitless. The depth is measured from average elevation, 2.5 km above sea level, which is $\tilde{2}.5$ km from the summit. The center of the source is at -78.47E and -1.46N, at 2 km west from the crater.

Parameters	Models	
	Mogi	Prolate
Depth [km]	14.5	7.4
ΔVolume [$Mm^3{\cdot}y^{-1}$]	7	2
Semi-major, minor axes [km]	-	2 by 0.2
Dip (0 = vertical prolate) [°]	-	25
Strike [°]	-	300
χ^2 [-]	0.7	0.5

further, we looked for transients in both the InSAR and GPS data (Fig. 7 and Tab 3), subdividing the data into the three periods identified by Hidalgo et al. (2015): a) May 13^{th} 2011-November 2^{nd} 2012 (16 SAR images); b) November 2^{nd} 2012-May 19^{th} 2013 (8 SAR images); c) May 19^{th} 2013-March 1^{st} 2014 (17 SAR images). LOS velocities are estimated as linear velocities from StaMPS results. For each period, the LOS velocities are referenced to the GPS sites as described by Muller et al. (2015). PS points with RMSE velocity greater than 10 mm·y^{-1} are disregarded. We attempted to integrate GPS and InSAR data for the three periods, but the velocities for such short periods are very noisy and the results are not particularly useful.

From May 2011 to November 2012, the dominant feature is the 'trap door' on the western flank, which moved away from the satellite at a rate of ∼10 mm·y^{-1} (label a, Fig. 7a). During Period 2, November 2012 to May 2013, there was deformation of ∼40 mm·y^{-1} towards the satellite, corresponding to a total of 22 mm in 6.5 months (label d, Fig. 7b). The deformation is centered on the western flank, mainly between 2800 m and 3600 m above sea level, consistent

Table 3: Average vertical velocities of the GPS sites and their respective RMSE for the July 2009 to July 2012 and from July 2012 then to July 2014. The trend due to the inflating prolate was subtracted from these velocities.

Site	July 2009-July 2012	July 2012-July 2014	Velocity change
		[mm·y^{-1}]	
BILB	1.3 ±2.0	-3.7 ±4.0	-4.6 ±4.5
CHON	1.1 ±2.8	-5.3 ±6.3	-6.4 ±6.4
MAZO	2.0 ±5.9	-7.3 ±7.6	-9.3 ±9.6
RETU	-5.9 ±13.2	-2.7 ±15.4	+3.2 ±20.3

with that observed in the stacked InSAR but better characterised by the PS analysis (Fig. 4a). Deformation toward the satellite is also visible on the northern flank (label e, Fig. 7b) but with velocity <30 mm·y^{-1}. During Period 3, May 2013 to March 2014, the deformation pattern is similar to Period 1: with the 'trap door' moving at a rate of ∼10 mm·y^{-1} (label f, Fig. 7c) and subsidence of ∼6 mm·y^{-1}on the southeastern flank (label h, Fig. 7c) .

Although located outside the deforming area, the GPS sites BILB, CHON and MAZO all show velocity changes in July 2012 (Fig. 3). After the long-term trend associated with the inflating prolate source is removed, the change in vertical velocity at BILB is -4.6 ±4.5 mm·y^{-1}, at CHON is -6.4±6.4 and at MAZO is 9.3±9.6 mm·y^{-1} (Tab. 3). These changes are close to the level of significance and well below the centimetric accuracy of the PS analysis. However, the velocity change corresponds with a change in the eruptive activity reported by Hidalgo et al. (2015), and occurs shortly before the rapid uplift of the western flank seen in the InSAR (label d, Fig. 7e).

5. Discussion

By combining InSAR and GPS data from Tungurahua volcano, Ecuador, we have identified both long-term magma flux into a mid-crustal reservoir and

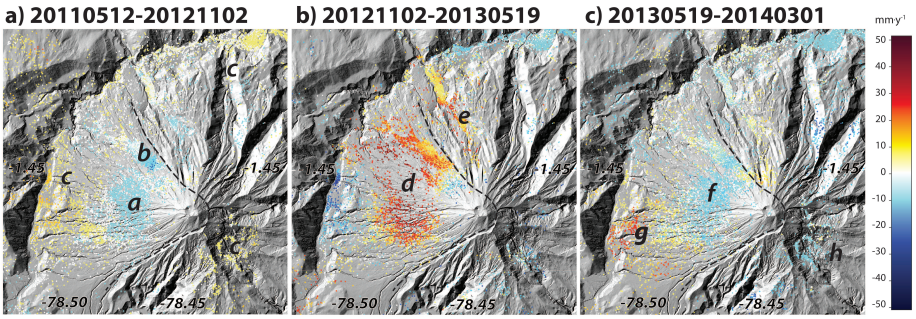

Figure 7: PS-InSAR LOS velocities for the 3 sub-periods as defined by Hidalgo et al. (2015). Linear velocities are estimated from StaMPS results. For each period, we reduce the LOS velocities as described by Muller et al. (2015). Positive values are deformation toward the satellite. The letters correspond to the features described in the text. .

episodic endogenous growth within the edifice. Our results agree with previous studies (Biggs et al., 2010a; Champenois et al., 2014; Hidalgo et al., 2015) but provide a more detailed view of the temporal and spatial behaviour of the plumbing system (Fig. 8). In this section, we discuss the implications of these results for the evolution of the magmatic system at Tungurahua, and for long-lived andesitic eruptions in general.

5.1. Mid-crustal magma supply and storage

InSAR data from Champenois et al. (2014), and our GPS-InSAR velocity field both show an uplift, however the magnitude and the spatial extent of the deformation differ, as well as the source parameters that generate the deformation. Champenois et al. (2014) found an optimal fit with a spherical source at a depth of 11.5 km below sea level while our study results suggest a tilted prolate spheroid source at 4.9 km below sea level. The two studies have a significant difference in coverage, spatial resolution and processing strategy: Champenois et al. (2014) used the single line-of-sight of ENVISAT data, which has a greater spatial extent (∼25 km) but detected only a few hundred persistent scatterers on the edifice, while we use a 3D velocity field with high resolution and thou-

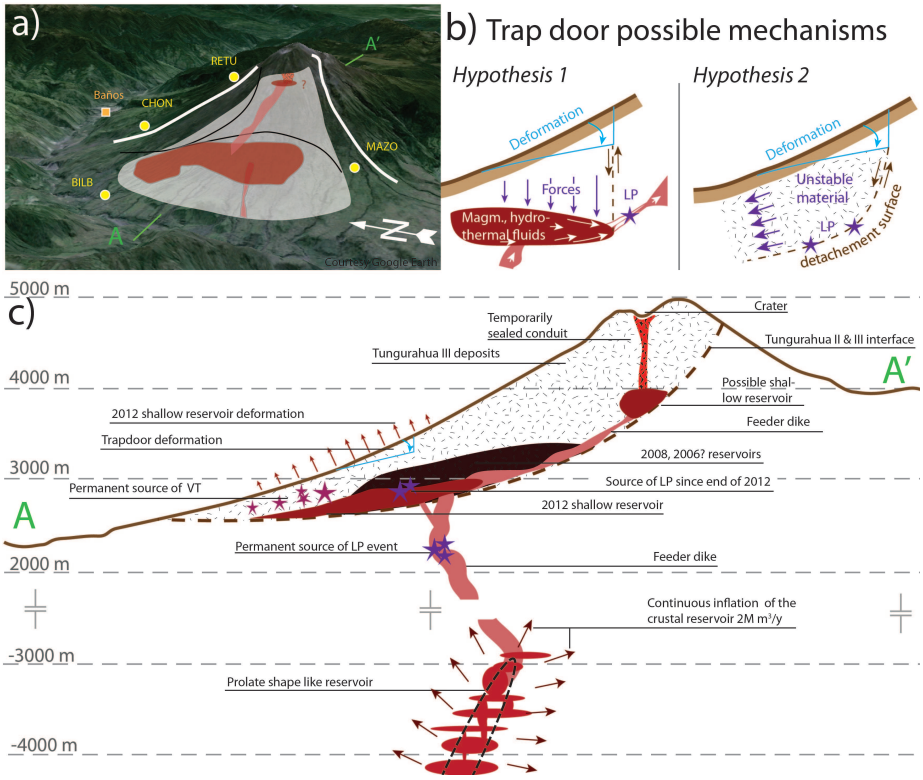

Figure 8: Proposed Tungurahua plumbing system and the time scale of its eruptive processes. a) oblique view of the volcano edifice and a global view of the current magma pathway. b) Possible mechanisms for generating the trap door subsidence c) detailed West-East cross section of the plumbing system.

sands of persistent scatterers on the edifice, but we have a smaller spatial extent (∼7 km). These differences strongly influence the trade-off in depth-volume for analytical models. To test whether a single source could be consistent with both datasets we compare (1) Champenois et al. (2014)'s observations to our spheroid prolate model and (2) our observations to Champenois et al. (2014)'s spherical model. The first comparison shows that when projected in the ENVISAT line-of-sight, the maximum deformation due to the inflating spheroid prolate is only half of the Champenois et al. (2014) observations (3.5 mm $\cdot y^{-1}$ versus up to 8 mm $\cdot y^{-1}$, RMSE $\pm$1.3 mm $\cdot y^{-1}$). The second comparison provides residuals even larger and reach up to 10 mm $\cdot y^{-1}$. In consequence, we suggest that the difference in depth and volume change between studies may, in fact, be due to the existence of two different sources and not due to the difference in coverage, spatial resolution and processing strategy.

Petrological studies based on geobarometry and phase equilibrium experiments are consistent with this analysis. Andújar et al. (2017) infer two reservoirs from the 2006 eruptive material: a deep reservoir at 400 MPa (12.5-13.5 km below sea level) and another reservoir at 200-250 MPa (5.5-7.5 km below m.s.l.). The deep reservoir is within uncertainty of the Champenois et al. (2014) model (12.5-13.5 $\approx$ 11.5 km below m.s.l.), while our model fits better with the shallower reservoir (5.5-7.5 $\approx$ 4.9 km below sea level), although we note that both geodetic depths are shallower than those estimated from petrology. Further investigations are required to formally assess this hypothesis and to understand the interaction between reservoirs.

In term of volume changes, Champenois et al. (2014) estimate a flux of 7 $Mm^3 \cdot y^{-1}$ in 2003-2009 and we estimate 2 $Mm^3 \cdot y^{-1}$ in 2011-2014 (this study). This decrease is also reported in the eruptive flux. In 2003-2009, the eruption rate was 33 $Mm^3 \cdot y^{-1}$ Dense Rock Equivalent (DRE) and in 2011-2014 in 2011-2014, it was only 5 $Mm^3 \cdot y^{-1}$ DRE (Mothes et al., 2015). Although Champenois et al. (2014) compared eruptive flux with volume change, they do not take into account compressibility, which can cause large differences in volumes (Kilbride

et al., 2016). The ratio between erupted volume and volume change at depth is:

$$V_e/\Delta V = -(1 + K_m/K_c) \quad (1)$$

where V_e is the erupted volume, ΔV the corresponding volume loss in the crustal reservoir, K_m is the magma compressibility and K_c is the compressibility of the magma reservoir (Mastin et al., 2008; Cervelli et al., 2010; Kilbride et al., 2016). Assuming a shear modulus of 3 GPa, the chamber compressibility, K_c, is 3.3×10^{-10} Pa^{-1} for a spherical chamber and 4×10^{-9} Pa^{-1} for a prolate chamber (e.g. Kilbride et al., 2016).

To estimate the magma compressibility, K_m, we follow the approach of Kilbride et al. (2016) using a melt water content of 3 wt% and a magma oxidation state of NNO+1 based on petrological observations from the 2006 eruption (Samaniego et al., 2011). An andesite melt containing 1000 ppm dissolved CO_2 would be vapour-undersaturated at 10 km depth, giving $K_m = 1.5 \times 10^{-10}$ Pa^{-1}, whereas, if the magma contained 5000 ppm CO_2, the presence of an exsolved vapour phase would increase the value of K_m to 2.5×10^{-10} Pa^{-1}. This gives volume ratios from 1.5 to 2, consistent with other observations from deeply sourced, large explosive eruptions (Kilbride et al., 2016).

Table 4 gives the equivalent subsurface and erupted volumes and rates once magma compressibility has been taken into account. From global observations of long-term fluxes, the ratio of intruded to extruded magma ranges between 1 to 10, with a mode of 2-3 and median of 5 (White et al., 2006). On shorter timescales, this ratio will vary through the eruption cycle, with high eruptive fluxes during eruptive periods balanced by intrusion during non-eruptive periods. During the eruption at Tungurahua, we find ratios ranging from 1.7 (2011-2014) to 1.8 (2003-2009), accounting for magma compressibility. The magma supply rate varies between 8.5 $Mm^3 \cdot y^{-1}$ (2011-2014) and 27 $Mm^3 \cdot y^{-1}$ (2003-2009) which is 6 to 18 time higher than the long term rate of Tungurahua's edifice growth (1.5 $Mm^3 \cdot y^{-1}$ (Hall et al., 1999)). Assuming all the magma re-

Table 4: Volume balance based on observations from estimates of eruptive volume at the surface (adjusted to Dense Rock Equivalent, DRE) and reservoir volume changes from surface deformation. The values in bold are based on the observations, while values in italics are the converted values using a compensating factor for compressibility. Magma supply rate/volume is the sum of the accumulated and the erupted values. The 2003-2009 values are from Champenois et al. (2014) and Mothes et al. (2015).

	In the crust (i.e. compressed)	At the surface (DRE)
2011-2014 rates		
Accumulation rate (this study)	**2±0.5 Mm^3·y^{-1}**	*3.5±0.7 Mm^3·y^{-1}*
Eruption rate (Mothes et al., 2015)	*2.9±0.7 Mm^3·y^{-1}*	**5±2.9 Mm^3·y^{-1}**
Supply rate	4.9±0.9Mm^3·y^{-1}	8.5±3.0 Mm^3·y^{-1}
2011-2014 volumes		
Accumulation	**6±0.9 Mm^3**	*10.5±1.3 Mm^3*
Eruption	*8.6±3.7 Mm^3*	**15±5 Mm^3**
Supply	14.6±3.8 Mm^3	26 ± 5.1 Mm^3
2003-2009 volumes		
Accumulation	**47±? Mm^3**	*82±? Mm^3*
Eruption	*52.5±7.4 Mm^3*	**105**±10 **Mm^3**
Supply	100±>7.4 Mm^3	187±>10 Mm^3

mains eruptible, the current supply rate (8.5 Mm^3·y^{-1}) would accumulate the volume of the August 2006 sub-Plinian eruption (50-100 Mm^3 (Eychenne et al., 2012; Mothes et al., 2015)) after 6-12 years.

The SO_2 loss during the 1999-2006 period required a degassed volume of 150 Mm^3 DRE (Arellano et al., 2008; Hidalgo et al., 2015), which is roughly two to three times greater than predicted by extrapolating the 2011-2014 rate of magma supply over 7 years (60 Mm^3 DRE). Excess SO_2 emission is a common feature of active volcanoes, and several processes are invoked to explain this,

including degassing of large bodies lying at shallow level; remobilisation of sulphur deposits and mixing between reduced and oxidized magmas (Rose et al., 1982; Witter et al., 2005; Kress, 1997). However, the 2003-2009 total supply volume (∼187 Mm^3 DRE), a similar period of time, is in agreement with the total degassed volume, which might indicate that the rate of magma supply is decreasing as the eruption continues, and SO_2 emission rates were higher for the 1999-2006 period.

5.2. Temporal changes in magmatic pathways

The eruption at Tungurahua is long-lived, but the pattern and characteristics of eruption are continually changing. Hidalgo et al. (2015) use the pattern of explosivity and gas flux to identify distinct phases of eruption, and here we use geodetic observations to investigate the differences in subsurface processes associated with changes in eruptive behaviour.

During Period 1 (July 2009-Nov 2011), the eruptions were explosive, with high gas flux and short eruption durations (Hidalgo et al., 2015) and the western flank subsided slowly, suggesting some of the erupted magma and/or gas was sourced from within the edifice. During Period 2 (Nov 2011 to Sept 2012), the eruptive activity was characterised by low explosivity (Strombolian) and low SO_2 flux (Mothes et al., 2015; Hidalgo et al., 2015). However, the subsidence continued, which might suggest that the change in behaviour was associated with a change in flux from deeper in the system.

Between July and December 2012, a clear transition in behavior occurred with 1) the resumption of strong episodic eruptions associated with high SO_2 flux and Vulcanian eruptions (Hidalgo et al., 2015); 2) uplift of the western flank by 2 cm, 3) an increase in the number of VT events on the western flank (Fig. 2) and 4) a decrease in vertical velocity at the GPS sites. These observations are consistent with an intrusion into the western flank.

From December 2012 to July 2014, the volcanic activity was characterized

by strong, short eruptions including 5 Vulcanian eruptions, separated by very short hiatuses showing low SO_2 flux (Hidalgo et al., 2015; Anderson et al., 2018). Both VT activity and co-eruptive $S0_2$ flux were high (Fig. 2) and the western flank was again subsiding. We conclude that magma and/or gas from the earlier intrusion may have helped feed the eruption which is also supported by tiltmeter observations (Neuberg et al., 2018).

5.3. Growth and deformation of the edifice

Although an order of magnitude smaller, the 2012 flank intrusion had a similar deformation pattern to one that accompanied the 2008 eruption (Biggs et al., 2010b). The repeated intrusions are likely exploiting a 3000 year old collapse scar on the western flank (Hall et al., 1999), which now presents a mechanical contrast between pre-collapse consolidated volcanic rock and recent deposits. Furthermore, the unconsolidated deposits above are characterized by low P-wave velocities (Molina et al., 2005) and likely amplify the signal further. We speculate that similar intrusions may have taken place during past periods of activity (e.g. 2003-2004, 2006), although geodetic measurements do not exist for those.

Both the 2008 and 2012 intrusions followed long periods of low but continuous activity, and culminated in a Vulcanian eruption (Biggs et al., 2010b; Mothes et al., 2015). In many ways, they are small-scale analogues of the cryptodome that formed prior to the eruption of Mt St Helens in 1980 (Dzurisin (2006), subsection 1.1.4). The geodetic observations alone cannot determine whether the intrusion represents shallow magma storage prior to a large eruption, or merely reflects an overall increase in magma pressure within the system. In either scenario, the deformation generated has significant value from a monitoring perspective, but whether an intrusion into Tungurahua's western flank could cause a collapse similar to that observed in the 1980 eruption of Mt St Helens remains to be seen.

Shallow deformation occurs on three other parts of Tungurahua's edifice, labelled 1, 2, 3a and 3b on Figure 5 and 6. The localised 'trap door' deformation pattern in the centre of the western flank (label 1 on Figure 5 and 6) occurs in a remote area, where no *in situ* observations have yet been made. However, long period events (< 4 Hz), triggered by short explosions prior to August 2006 eruption, formed a cluster ∼500 m below this area of subsidence (Figure 11b in Palacios et al. (2015)). These events are traditionally considered to indicate fluid movement and, although the depth is not well constrained by the monopolar source model, the presence of a cluster just beneath the deformation strongly suggests they are related. Fluids, whether magmatic or hydrothermal, can generate trap door-like deformation by applying differential stresses during restricted circulation or emptying (e.g. Amelung et al., 2000) (Fig. 8b). Alternatively, LP events can be caused by creep within an inelastic medium (Bean et al., 2014) and the 'trap-door' deformation could be the surface expression of a rotational detachment (e.g. Ruch et al., 2010). We estimate the depth of the listric failure plane to be on the order of hundreds of meters (Dula Jr, 1991), corresponding to the depth of the LP events. In either case, this feature may indicate a potential site for lateral eruptions and hence future hazards for the downstream communities.

Subsidence NW of the active crater (label 2 in Fig 5) affects the top 900 m of Tungurahua's edifice and may be associated with the surface response to the loading of the recently erupted material, as observed elsewhere (e.g. Lu and Dzurisin, 2014; Ebmeier et al., 2014; Muller et al., 2015). Subsidence on the north-eastern and the southern flank (label 3a and 3b), is constrained by a few PS, and may be related to localised slope instabilities in unvegetated area.

6. Conclusion

This study combines high-resolution InSAR and GPS at Tungurahua Volcano Ecuador between 2011 and 2014. The combination of InSAR and GPS produces a 3-D displacement field in an absolute reference frame which allows us to investigate the source geometry of the deep reservoir in more detail than previous studies. An asymmetric deformation pattern with a high ratio of horizontal to vertical motion favours a tilted prolate spheroid located ∼7.5 km beneath the average surface. We compare the rate of accumulation within the edifice to that of eruption, accounting for magma compressibility, and find that during this period, slightly more than half of the magma supplied to the reservoir reached the surface.

The use of high resolution TerraSAR-X data with Persistent Scatterer methods enables us to study deformation of the edifice itself, and we detect an intrusion into the western flank, similar to the one that occurred during the 2008 eruption (Biggs et al., 2010b), but smaller in magnitude. The intrusions occur within the edifice, likely along the collapse scar between consolidated volcanic rock and recent deposits. Both intrusions accompanied Vulcanian eruptions and changes in eruptive behaviour, suggesting they may be useful indicators of changes in the magmatic system. We also detect a localised area of subsidence around 3300 m above sea level, that corresponds to the location of shallow long period seismicity, and may represent a potential lateral vent site.

These observations have implications for the understanding of the plumbing systems of long-lived stratovolcano eruptions such as Tungurahua, Ecuador, with consequences for short-term hazard assessments. In particular, we demonstrate the advantages of statistical methods for improving the signal to noise ratio of both InSAR and GPS data, integration of multiple geodetic datasets and comparisons with other monitoring information.

Acknowledgments

This work received financial support from the University of Bristol, the NERC/ESRC thematic programme STREVA grant number NE/J020052/1, the NERC Centre for the Observation and Modeling of Earthquakes, Volcanoes and Tectonics (COMET) as well as from the OVSICORI-UNA and the SOGeod project. SKE is supported by an Early Career Fellowship from the Leverhulme Trust and the European Space Agency. We thank Jeff Freymueller and one anonymous reviewer for their thoughtful comments.

References

Alvarado, A., Ruiz, M., Mothes, P., Yepes, H., Segovia, M., Vaca, M., Ramos, C., Enríquez, W., Ponce, G., Jarrín, P., et al., 2018. Seismic, volcanic, and geodetic networks in ecuador: Building capacity for monitoring and research. Seismological Research Letters 89, 432–439.

Amelung, F., Jónsson, S., Zebker, H., Segall, P., 2000. Widespread uplift and trapdoor faulting on Galapagos volcanoes observed with radar interferometry. Nature 407, 993–996.

Anderson, J., Johnson, J., Steele, A., Ruiz, M., Brand, B., 2018. Diverse eruptive activity revealed by acoustic and electromagnetic observations of the 14 july 2013 intense vulcanian eruption of tungurahua volcano, ecuador. Geophysical Research Letters 45. doi:https://doi.org/10.1002/2017GL076419.

Andújar, J., Martel, C., Pichavant, M., Samaniego, P., Scaillet, B., Molina, I., 2017. Structure of the plumbing system at tungurahua volcano, ecuador: Insights from phase equilibrium experiments on july–august 2006 eruption products. Journal of Petrology 58, 1249–1278. doi:10.1093/petrology/egx054.

Arellano, S., Hall, M., Samaniego, P., Le Pennec, J.L., Ruiz, A., Molina, I., Yepes, H., 2008. Degassing patterns of Tungurahua volcano (Ecuador) during

the 1999–2006 eruptive period, inferred from remote spectroscopic measurements of SO_2 emissions. Journal of Volcanology and Geothermal Research 176, 151–162.

Battaglia, M., Cervelli, P.F., Murray, J.R., 2013. Modeling crustal deformation near active faults and volcanic centers: a catalog of deformation models. US Geological Survey Techniques and Methods , 13–B1.

Bean, C.J., De Barros, L., Lokmer, I., Métaxian, J.P., OBrien, G., Murphy, S., 2014. Long-period seismicity in the shallow volcanic edifice formed from slow-rupture earthquakes. Nature geoscience 7, 71–75.

Berardino, P., Fornaro, G., Lanari, R., Sansosti, E., 2002. A new algorithm for surface deformation monitoring based on small baseline differential SAR interferograms. Geoscience and Remote Sensing, IEEE Transactions on 40, 2375–2383.

Biggs, J., Ebmeier, S., Aspinall, W., Lu, Z., Pritchard, M., Sparks, R., Mather, T., 2014. Global link between deformation and volcanic eruption quantified by satellite imagery. Nature Communications 5:3471.

Biggs, J., Lu, Z., Fournier, T., Freymueller, J.T., 2010a. Magma flux at Okmok volcano, Alaska, from a joint inversion of continuous GPS, campaign GPS, and interferometric synthetic aperture radar. Journal of Geophysical Research: Solid Earth 115.

Biggs, J., Mothes, P., Ruiz, M., Amelung, F., Dixon, T., Baker, S., Hong, S.H., 2010b. Stratovolcano growth by co-eruptive intrusion: The 2008 eruption of Tungurahua Ecuador. Geophysical Research Letters 37, L21302. doi:10.1029/2010GL044942.

Cayol, V., Cornet, F.H., 1998. Effects of topography on the interpretation of the deformation field of prominent volcanoes: Application to Etna. Geophysical Research Letters 25, 1979–1982.

Cervelli, P.F., Fournier, T.J., Freymueller, J.T., Power, J.A., Lisowski, M., Pauk, B.A., 2010. Geodetic constraints on magma movement and withdrawal during the 2006 eruption of Augustine volcano. U.S. Geological Survey Professional Paper 415, 427–452.

Champenois, J., Pinel, V., Baize, S., Audin, L., Jomard, H., Hooper, A., Alvarado, A., Yepes, H., 2014. Large-scale inflation of Tungurahua volcano (Ecuador) revealed by Persistent Scatterers SAR interferometry. Geophysical Research Letters 41, 5821–5828.

Dula Jr, W.F., 1991. Geometric models of listric normal faults and rollover folds (1). AAPG Bulletin 75, 1609–1625.

Dzurisin, D., 2006. Volcano Deformation, Geodetic monitoring techniques. Springer-Verlag Berlin Heidelberg New York, USA.

Ebmeier, S., Biggs, J., Mather, T., Amelung, F., 2013. Applicability of InSAR to tropical volcanoes: insights from Central America. Geological Society, London, Special Publications 380, 15–37.

Ebmeier, S.K., Biggs, J., Muller, C., Avard, G., 2014. Thin-skinned mass-wasting responsible for widespread deformation at Arenal volcano. Frontiers in Earth Science 2, 35.

Eychenne, J., Le Pennec, J.L., Ramón, P., Yepes, H., 2013. Dynamics of explosive paroxysms at open-vent andesitic systems: High-resolution mass distribution analyses of the 2006 Tungurahua fall deposit (Ecuador). Earth and Planetary Science Letters 361, 343–355.

Eychenne, J., Le Pennec, J.L., Troncoso, L., Gouhier, M., Nedelec, J.M., 2012. Causes and consequences of bimodal grain-size distribution of tephra fall deposited during the August 2006 Tungurahua eruption (Ecuador). Bulletin of Volcanology 74, 187–205.

Ferretti, A., Prati, C., Rocca, F., 2001. Permanent scatterers in SAR interferometry. Geoscience and Remote Sensing, IEEE Transactions 39, 8–20.

Gottsmann, J., Odbert, H., 2014. The effects of thermomechanical heterogeneities in island arc crust on time-dependent pre-eruptive stresses and the failure of an andesitic reservoir. Journal of Geophysical Research: Solid Earth 119, 4626–4639.

Guglielmino, F., Bignami, C., Bonforte, A., Briole, P., Obrizzo, F., Puglisi, G., Stramondo, S., Wegmüller, U., 2011. Analysis of satellite and in situ ground deformation data integrated by the SISTEM approach: The April 3, 2010 earthquake along the Pernicana fault (Mt. Etna-Italy) case study. Earth and Planetary Science Letters 312, 327–336.

Hall, M., Robin, C., Beate, B., Mothes, P., Monzier, M., 1999. Tungurahua volcano, Ecuador: structure, eruptive history and hazards. Journal of Volcanology and Geothermal Research 91, 1–21. doi:{10.1016/S0377-0273(99)00047-5}.

Herring, T., King, R., McClusky, S., 2010. GAMIT Reference Manual, GPS Analysis at MIT. 10.4 ed. Department of Earth, Atmospheric, and Planetary Sciences Massachusetts Institute of Technology.

Hidalgo, S., Battaglia, J., Arellano, S., Steele, A., Bernard, B., Bourquin, J., Galle, B., Arrais, S., Vásconez, F., 2015. SO_2 degassing at Tungurahua volcano (Ecuador) between 2007 and 2013: transition from continuous to episodic activity. Journal of Volcanology and Geothermal Research .

Hooper, A., Pedersen, R., Sigmundsson, F., 2009. Constraints on magma intrusion at Eyjafjallajökull and Katla volcanoes in Iceland, from time series SAR interferometry. The VOLUME Project–Volcanoes: Understanding Subsurface Mass Movement. Dublin: University College , 13–24.

Hooper, A., Segall, P., Zebker, H., 2007. Persistent scatterer interferometric synthetic aperture radar for crustal deformation analysis, with application to Volcán Alcedo, Galápagos. Journal of Geophysical Research: Solid Earth 112, B07407. doi:doi:10.1029/2006JB004763.

Kelfoun, K., Samaniego, P., Palacios, P., Barba, D., 2009. Testing the suitability of frictional behaviour for pyroclastic flow simulation by comparison with a well-constrained eruption at Tungurahua volcano (Ecuador). Bulletin of Volcanology 71, 1057–1075.

Kilbride, B.M., Edmonds, M., Biggs, J., 2016. Observing eruptions of gas-rich compressible magmas from space. Nature Communications 7.

Kress, V., 1997. Magma mixing as a source for Pinatubo sulphur. Nature 389, 591–593.

Kumagai, H., Yepes, H., Vaca, M., Caceres, V., Naga, T., Yokoe, K., Imai, T., Miyakawa, K., Yamashina, T., Arrais, S., et al., 2007. Enhancing volcano-monitoring capabilities in ecuador. Eos, Transactions American Geophysical Union 88, 245–246. doi:10.1029/2007EO230001.

Lu, Z., Dzurisin, D., 2014. InSAR imaging of Aleutian volcanoes: monitoring a volcanic arc from space. Springer Science & Business Media, Berlin Germany.

Mastin, L.G., Roeloffs, E., Beeler, N.M., Quick, J.E., 2008. Constraints on the size, overpressure, and volatile content of the Mount St. Helens magma system from geodetic and dome-growth measurements during the 2004-2006+ eruption. US Geological Survey Professional Paper 1750, 461–488.

Molina, I., Kumagai, H., Le Pennec, J.L., Hall, M., 2005. Three-dimensional p-wave velocity structure of tungurahua volcano, ecuador. Journal of Volcanology and Geothermal Research 147, 144–156.

Mothes, P., Hall, M.L., Samaniego, P., Ramn, P., Molina, C.L., Yepes, H., Le Pennec, J.L., Ruiz, G., Andrade, D., Enriquez, W., Garcia, A., Eissen, J.P., Hidalgo, S., Monzier, M., 2004. Monitoring of a drawn-out episodic eruption, Tungurahua volcano, Ecuador. IAVCEI General Assembly, Pucon, Chile .

Mothes, P.A., Yepes, H.A., Hall, M.L., Ramón, P.A., Steele, A.L., Ruiz, M.C., 2015. The scientific–community interface over the fifteen-year eruptive episode of Tungurahua Volcano, Ecuador. Journal of Applied Volcanology 4, 1–15.

Muller, C., del Potro, R., Biggs, J., Gottsmann, J., Ebmeier, S.K., Guillaume, S., Cattin, P.H., Van der Laat, R., 2015. Integrated velocity field from ground and satellite geodetic techniques: application to Arenal volcano. Geophysical Journal International 200, 863–879.

Neuberg, J.W., Collinson, A.S., Mothes, P.A., Ruiz, M.C., Aguaiza, S., 2018. Understanding cyclic seismicity and ground deformation patterns at volcanoes: Intriguing lessons from tungurahua volcano, ecuador. Earth and Planetary Science Letters 482, 193–200.

Odbert, H.M., Ryan, G.A., Mattioli, G.S., Hautmann, S., Gottsmann, J., Fournier, N., Herd, R.A., 2014. Volcano geodesy at the Soufrière Hills Volcano, Montserrat: a review. Geological Society, London, Memoirs 39, 195–217.

Palacios, P., Kendall, J.M., Mader, H., 2015. Site effect determination using seismic noise from Tungurahua volcano (Ecuador): implications for seismo-acoustic analysis. Geophysical Journal International 201, 1084–1100.

Parker, A.L., Biggs, J., Walters, R.J., Ebmeier, S.K., Wright, T.J., Teanby, N.A., Lu, Z., 2015. Systematic assessment of atmospheric uncertainties for InSAR data at volcanic arcs using large-scale atmospheric models: Application to the Cascade volcanoes, United States. Remote Sensing of Environment 170, 102–114.

Phillipson, G., Sobradelo, R., Gottsmann, J., 2013. Global volcanic unrest in the 21st century: an analysis of the first decade. Journal of Volcanology and Geothermal Research 264, 183–196.

Pinel, V., Hooper, A., De la Cruz-Reyna, S., Reyes-Davila, G., Doin, M., Bascou, P., 2011. The challenging retrieval of the displacement field from InSAR

data for andesitic stratovolcanoes: Case study of Popocatepetl and Colima Volcano, Mexico. Journal of Volcanology and Geothermal Research 200, 49–61.

Riddick, S., Schmidt, D., Deligne, N., 2012. An analysis of terrain properties and the location of surface scatterers from persistent scatterer interferometry. ISPRS Journal of Photogrammetry and Remote Sensing 73, 50–57.

Rose, W., Stoiber, R., Malinconico, L., 1982. Eruptive gas compositions and fluxes of explosive volcanoes: budget of S and Cl emitted from Fuego volcano, Guatemala, in: Andesites. Wiley New York, NY, pp. 669–676.

Rosen, P.A., Hensley, S., Peltzer, G., Simons, M., 2004. Updated repeat orbit interferometry package released. Eos, Transactions American Geophysical Union 85, 47–47.

Ruch, J., Acocella, V., Storti, F., Neri, M., Pepe, S., Solaro, G., Sansosti, E., 2010. Detachment depth revealed by rollover deformation: An integrated approach at Mount Etna. Geophysical Research Letters 37.

Samaniego, P., Le Pennec, J.L., Robin, C., Hidalgo, S., 2011. Petrological analysis of the pre-eruptive magmatic process prior to the 2006 explosive eruptions at Tungurahua volcano (Ecuador). Journal of Volcanology and Geothermal Research 199, 69–84.

Samsonov, S., Tiampo, K., 2006. Analytical optimization of a DInSAR and GPS dataset for derivation of three-dimensional surface motion. Geoscience and Remote Sensing Letters, IEEE 3, 107–111.

Sparks, R., 2003. Forecasting volcanic eruptions. Earth and Planetary Science Letters 210, 1–15.

Trasatti, E., Giunchi, C., Bonafede, M., 2003. Effects of topography and rheological layering on ground deformation in volcanic regions. Journal of Volcanology and Geothermal Research 122, 89–110.

White, S.M., Crisp, J.A., Spera, F.J., 2006. Long-term volumetric eruption rates and magma budgets. Geochemistry, Geophysics, Geosystems 7. doi:doi:10.1029/2005GC001002.

Witter, J., Kress, V., Newhall, C., 2005. Volcán Popocatépetl, Mexico. Petrology, magma mixing, and immediate sources of volatiles for the 1994–present eruption. Journal of Petrology 46, 2337–2366.